Research Article

Evaluation of Streamwise Waveform on a High-Speed Water Jet by Detecting Trajectories of Two Refracted Laser Beams

Kazuhiro Itoh, Yasuo Iwata, Hiroshige Kumamaru, and Yuji Shimogonya

Department of Mechanical and System Engineering, University of Hyogo, 2167 Shosha, Himeji, Hyogo 671-2280, Japan

Correspondence should be addressed to Kazuhiro Itoh, itoh@eng.u-hyogo.ac.jp

Free surface fluctuations on a high-speed water jet were measured by a laser beam refraction technique. This method can be used to obtain quantitative time-series data on local surface fluctuations. The developed system employs two pulsed laser diodes, and it uses a high-speed optical sensor to detect the instantaneous positions of the laser beams that are refracted at the free surface. Fluctuations in the slope angle are measured at two locations separated by 1.27 mm. The wave speed of each free surface wave, which is determined by the zero-upcrossing method, is experimentally evaluated by the cross-correlation method. A two-dimensional waveform is obtained by integrating the slope angle data. The local mean wavelength and mean wave steepness are evaluated for average jet velocities up to $U = 10$ m/s. Streamwise waveforms of the high-speed water jet at several locations exhibit appreciable asymmetry and have steep profiles.

1. Introduction

The material flux through a gas/liquid interface, the heat transfer rate, and the interfacial friction vary significantly depending on whether waves are generated on the free surface or not [1, 2]. Consequently, much effort has been devoted to measuring free surface waves and to determining their statistical properties using electronic and optical measurement techniques.

With the exception of flush-mounted probes embedded in channel walls (which can perform measurements only in a limited range of liquid depths), electric level gauges generally have intrusive electrodes [3, 4]. Nonintrusive optical techniques are much more preferable since they do not penetrate the surface.

Of these nonintrusive optical techniques, we have focused on time-series measurements of the local properties (i.e., absorption, reflection, and refraction) of a narrow laser beam. This approach can provide high-frequency data for slope angle and liquid depth at a fixed point on a free surface, making it more suitable for evaluating the statistical properties of free surface waves than conventional optical methods (e.g., colorimetry [5–7] and moiré topography

[8, 9]); most conventional methods can obtain only relative information about free surface fluctuations.

Lilleleht and Hanratty [10] measured liquid height fluctuations from light intensity variations. They used a chopped light beam that passed through a stratified wavy flow containing methylene blue dye to evaluate the root-mean-square displacement and obtain frequency spectra. However, this light absorption method is susceptible to noise for long light paths. Furthermore, the ratio of fluid depth to wave height is generally limited.

Hashimoto and Suzuki [11] obtained frequency spectra of a thin liquid film by detecting the displacement of reflected and refracted laser beams. Yoshino et al. [12] measured the wavy water surface on a rotating drum by following the laser beam reflected at the free surface. They used a one-dimensional (1D) photodiode array to measure the beam displacement and so could achieve high data acquisition rates of up to 20 kHz. However, to adapt this method for a general free surface, the 2D position of a light beam on a photodiode must be measured. Duke et al. [13] used a 2D photodiode array as a light sensor and obtained slope angle fluctuation data from a stratified wavy free surface. In this measurement, the measurement range of the free surface

slope angle is strongly restricted by the limited area of the optical receiver due to problems with high-speed scanning of photodiode arrays. Consequently, the response frequency of Duke's experiment was limited to 285 Hz.

To overcome this limitation, we employ a high-speed single-plane photodiode as the light detector. Previously, we achieved a response rate of 33 kHz for free surface slope angle measurements, and we evaluated the spectral characteristics of free surface fluctuations [14, 15] of a high-speed (up to 20 m/s) water jet. This kind of detector has recently been used to measure surface gradients. Savelsberg et al. [16, 17] and Snouck et al. [18] measured 2D slope angle profiles on wavy free surfaces by single laser scanning at a scanning frequency of 2 kHz.

In the present study, by extending the light sources, we measure fluctuations in the local slope angle at two locations on a wavy surface. By increasing the number of measurement locations, the wave velocity can be experimentally evaluated using the cross-correlation technique. Although we have evaluated waveforms from slope angle data in a previous study [14] using a single continuous-wave laser as the light source, information about the wave velocity was limited in a speculation by a linear stability theory concerning with the laminar shear layer underneath the free surface. Moreover, linear theory is not applicable when the average jet velocity exceeds ~8 m/s since the transition from a laminar boundary layer to a turbulent boundary layer occurs at the nozzle exit in the experimental conditions we use [14, 15]. Therefore, this study evaluates the nonlinear and unpredictable free surface fluctuations for higher jet velocities (up to 10 m/s; cf. ≤ 5 m/s in the previous study) by extending the experimental arrangement of the previous study [19].

Pulsed operation is required to prevent photocurrents overlapping when a single photodiode is used to detect multiple light beams. Data processing is used in this study to obtain the positions of the two pulsed laser beams on the diode. The wave velocity and spatial elevation of the free surface are determined for each wave period by applying the zero-upcrossing method to time-series slope angle data. The statistical properties of the mean wave steepness and the spatial waveform obtained by integrating the slope angle data are reported.

2. Experiment

Figure 1 shows a schematic diagram of the test section, which is made from transparent acrylic resin. The system uses water as the working fluid at room temperature and atmospheric pressure. A plane water jet is generated from a 2D convergent nozzle, and it flows along a flat horizontal wall. The nozzle exit height is 10 mm and its width is 100 mm. The jet width is fixed by the sidewalls and the jet free surface is open to the atmosphere to permit optical measurements and visual observations. The x-axis lies in the streamwise direction, the y-axis is in the spanwise direction, and the z-axis is vertical (see Figure 1).

Figure 1 also shows the optical arrangement used to measure free surface waves. Two laser beams illuminate
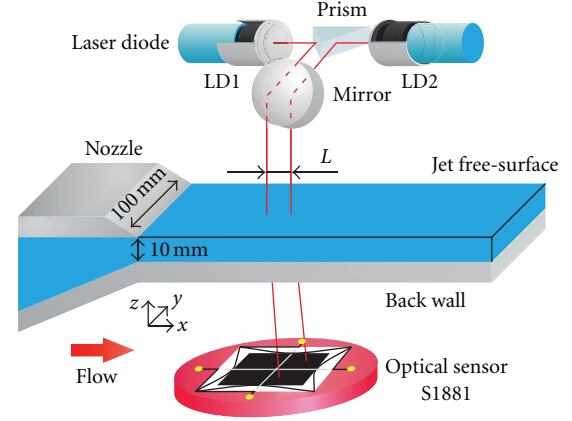

Figure 1: Schematic diagram of test section and optical system.

the water surface vertically. Two pulsed laser diodes (Premier LC, Global Laser, Gwent, UK; wavelength: 655 nm; output power: 1 mW; maximum pulse rate: 300 kHz) are employed as light sources. A focusing lens (focal length: 150 mm) and cylindrical collimator (diameter: 1 mm; length: 3 mm) reduce the beam diameter at the water surface to ≤24 μm. The two laser beams are separated by a distance $L = 1.27$ mm on the free surface in the streamwise direction. The distance L is adjusted to be smaller than the mean wavelength at the typical measurement locations to reduce deformation of free surface waves when they pass the two illuminated positions. The lasers are alternately pulsed at a frequency of 40 kHz. The output signal sampling rate was limited to 40 kHz in the present experiment. The pulse frequency is determined by the dynamic response of the optical sensor (see Section 4). Since the laser beam size on the jet free surface (24 μm) is much smaller than the typical mean wavelength (≥0.47 mm), the limited time response of the alternating illumination mainly restricts the measurable range of waves in the present experiment.

Experiments were performed using cross-sectional average velocities at the nozzle exit of $U = 6, 7, 8, 9$ and 10 m/s. U is calculated from the flow rate, which was measured using an orifice flow meter (FLG-N, Nippon Flow Cell, Tokyo, Japan) upstream of the test section. The accuracy of the flow rate measurements was less than ±2.0% (±0.2 m/s for the cross-sectional velocity). Optical measurements of the free surface were performed at 45 locations between $x = 0.64$ and 80.64 mm for each cross-sectional average velocity condition. The optical system and sensors were translated along the central axis of the test section by high-precision motion stages. The measurement location is indicated by a halfway between the two laser beams in the streamwise direction.

The present approach evaluates the free surface slope angle from the refracted laser beam position on the diode. Figure 2 shows the relationship between the beam displacement on the optical sensor r_x and the local slope angle θ_x of the free surface. The beam is refracted by the water surface and passes through the water, the transparent back wall, and air before reaching the optical sensor (S1881, Hamamatsu Photonics, Shizuoka, Japan). The streamwise displacement

along the x-axis is expressed in terms of the local slope angle by

$$r_x = D_w \tan(\theta_x - \theta_w) + D_b \tan\theta_b + D_a \tan\theta_a, \quad (1)$$

where D_w and D_b are, respectively, the thicknesses of the jet and the transparent back wall (10 mm), and D_a is the distance from the back wall to the sensor (20 mm). θ_w, θ_b, and θ_a are the angles of the refracted beam at the three interfaces; they obey Snell's law of refraction:

$$\frac{\sin\theta_x}{\sin\theta_w} = \frac{n_w}{n_a}, \qquad \frac{\sin(\theta_x - \theta_w)}{\sin\theta_b} = \frac{n_b}{n_w}, \qquad \frac{\sin\theta_b}{\sin\theta_a} = \frac{n_a}{n_b}, \quad (2)$$

where n_w, n_b, and n_a are the refractive indices of water, acrylic resin, and air, respectively [13].

The instantaneous free surface slope angle θ_x is calculated by substituting the detected displacement r_x into (1) and (2). The solution for θ_x in (1) and (2) can be obtained by an iterative numerical method; however, this requires a long data processing time. The relation between r_x and θ_x is determined by least-squares fitting (1) and (2) using a fifth-order polynomial, and it is used to calculate θ_x. Figure 3 shows the fifth-order polynomial curve together with calibration data that was obtained experimentally by inclining a 0.15-mm-thick cover glass on the stationary water surface. The base data for least-squares fitting, which are the numerical solutions of (1) and (2), are not shown in Figure 3 because they coincide almost exactly with the solid line in the figure. The theoretical curve deviates by less than ± 0.02 rad from the calibration data. We also confirmed that fluctuations in the jet thickness D_w have only a small effect on the measured value of θ_x. For example, a 10% (=1 mm) increase in the jet thickness (which is four times the typical mean wave height) shifts the theoretical curve by only 0.01 rad under the present experimental conditions (see the dotted line in Figure 3). The overall uncertainly of this measurement is evaluated to be less than ± 0.03 rad. The maximum slope angle measurable by this method depends on the light path length, the refractive indices of the materials, and the optical sensor size; it was ± 0.80 rad for the present geometry.

The present detector can measure the 2D displacement (r_x, r_y) of a laser beam. It is necessary to greatly reduce the probability of beams missing the detection area. However, since the jet velocity far exceeds the phase velocity of the waves in the present experimental conditions, the waves move very little in the spanwise direction during the short period when they pass through the measurement location. This makes it difficult to discuss the spanwise waveform from the displacement data of r_y, whereas basic statistical parameters can be measured qualitatively (e.g., the root-mean-square deviation (RMSD) of r_y in Figure 11 of [13]). Consequently, the present study focuses on evaluating the gradient in the streamwise direction of the jet free surface.

3. Data Acquisition and Processing

The optical sensor (S1881) used in this experiment consists of a single pin photodiode. It can detect the 2D displacement
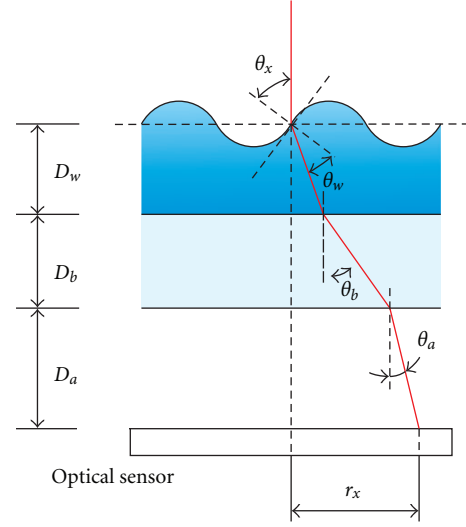

Figure 2: Schematic diagram showing relationship between free surface slope angle and displacement on optical sensor.

○ Calibration data
—— Least-square fitting of (1) and (2) (fifth-order polynomial curve)
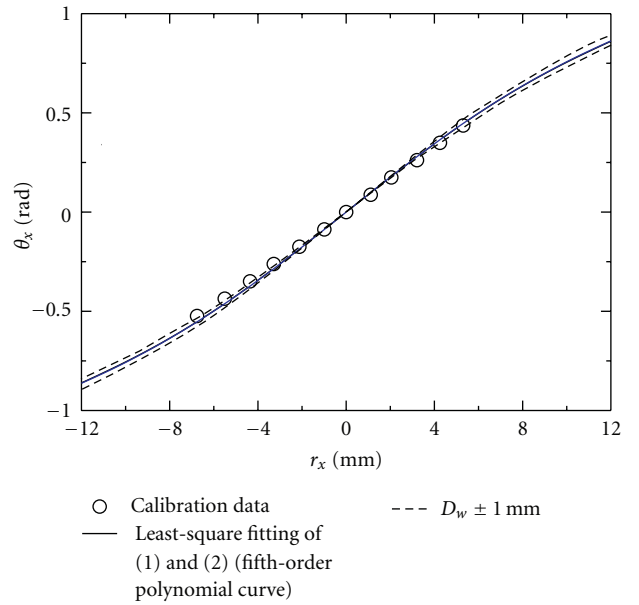--- $D_w \pm 1$ mm

Figure 3: Plot of free surface slope angle as a function of displacement on optical sensor.

of a beam on its detection area. As shown in Figure 4, the beam induces photocurrent signals X_1 and X_2 in the streamwise direction and Y_1 and Y_2 in the spanwise direction by the photovoltaic effect. These signals are amplified by a high-response op-amp (T-IVA001B, Turtle Industry, Ibaraki, Japan) and are sampled independently. The instantaneous displacements r_x and r_y are calculated using

$$r_x = \frac{L_x}{2} \frac{(X_2 + Y_1) - (X_1 + Y_2)}{X_1 + X_2 + Y_1 + Y_2},$$

$$r_y = \frac{L_y}{2} \frac{(X_2 + Y_2) - (X_1 + Y_1)}{X_1 + X_2 + Y_1 + Y_2}, \quad (3)$$

where $L_x = L_y = 26$ mm are the side lengths of the detection area (including the nonactive area) of the optical sensor.

This single-photodiode sensor is suitable for the present measurements since it has a maximum response frequency of 300 kHz for a continuous beam. However, if two or more beams are simultaneously illuminated on its detection area, it detects only the median point of each beam due to overlapping of the induced photocurrents. Therefore, we turned on the two laser diode beams alternately to prevent them from simultaneously illuminating the detection area. Although this switching operation generates a delay between the data acquisition of the two laser diodes, the dominant time lag of the cross-correlation coefficient can be determined by comparing the acquisition time of each data point with the switching data for the diodes. Therefore, the signals that control the timing of laser beams are recorded at a higher rate of 400 kHz simultaneously with the output voltage of the optical sensor.

The cross-correlation coefficient $R(\tau)$ is represented in terms of fluctuations in the slope angles θ_{x1} and θ_{x2},

$$R(\tau) = \frac{\overline{\theta_{x1}(t)\theta_{x2}(t+\tau)}}{\sqrt{\overline{\theta_{x1}^2}}\sqrt{\overline{\theta_{x2}^2}}}, \qquad (4)$$

where τ is the time lag due to the spatial separation between the measurement locations. The wave speed c_x is evaluated from the dominant time lag τ_a, which is related to the maximum cross-correlation coefficient by $c_x = L/\tau_a$. Since each wave on the free surface is considered to propagate at a different wave speed, τ_a can be calculated for individual waves, which are separated from the time-series data for θ_{x1} using the zero-upcrossing method. The zero-upcrossing method is commonly used to determine the wave period in time-domain analysis of irregular or randomly fluctuating data [20]. The wave period is determined as the time interval between successive crossings of the mean level of the data in the upward direction (Section 4 gives an example of crossings in the measured slope angle data).

The spatial waveform is reconstructed as follows. Denoting the free surface shape by $z = \eta_x(x)$, the local slope angle θ_x in the streamwise direction can be written as

$$\tan\theta_x = \frac{\partial\eta_x}{\partial x} = \frac{\partial\eta_x}{\partial t} \cdot \frac{\partial t}{\partial x}, \qquad (5)$$

where $\partial x/\partial t$ is the speed of the free surface wave that passes through the measurement point. If waves are assumed to propagate with frozen profiles when passing through the measurement point, the wave shape η_x is obtained by integrating (5) with respect to time:

$$\eta_x = \int_{\text{wave}} \left(\frac{\partial x}{\partial t}\right) \cdot \tan\theta_x \, dt = \int_{\text{wave}} c_x \cdot \tan\theta_x \, dt, \qquad (6)$$

where the subscript *wave* denotes an individual wave; the frozen profile is assumed to last for only a short period as the wave passes the measurement location. Thus, η_x is calculated by numerically integrating (6) by substituting the evaluated wave speed c_x for individual wave periods. The wave height h is obtained from the interval between the maximum and
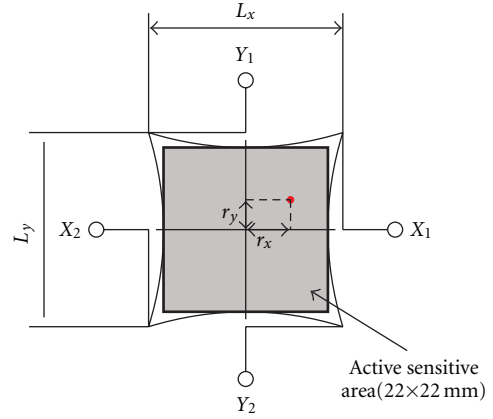

Figure 4: Output signals of optical sensor, S1881.

minimum values of η_x. The wavelength λ is calculated as the product of c_x and each wave period for θ_x. Examples of estimated results for η_x are given below (see Figure 11) after first considering the threshold value to confirm the validity of assumption of the frozen profile in the cross-correlation method.

4. Results

Figure 5 shows typical data for beam displacements r_x and the signals for controlling the switching of the laser diodes. Figure 5(a) shows examples of time intervals that include two wave periods. The shorter interval between 0.4000 and 0.5000 ms is magnified in Figure 5(b). The control signal voltage (shown in the lower figures in Figures 5(a) and 5(b)) is positive when the upstream laser (LD1) is switched on and the downstream laser (LD2) is switched off. The streamwise displacements of the two lasers are intermingled in the raw data, as shown by the open circles in the upper figures of Figures 5(a) and 5(b). Moreover, transition signals appear when the two lasers are alternately illuminated. The transitional motion is bounded by the horizontal arrows between 0.4500 and 0.5000 ms in Figure 5(b). This signal is generated by the intermediate output of the optic sensor, while the laser diodes alternate. It has a much shorter period than the waves. Similar signals were observed in the preliminary test when a stationary nonfluctuating water surface was measured. This temporal output is considered to arise from jumping of the beam positions or the variation in the beam intensity during switching. Consequently, only signals immediately prior to switching are used for statistical analysis. These reliable data are indicated by the red and blue solid circles in Figures 5(a) and 5(b). The acquisition frequency for this reliable data was chosen such that the output signal from the present sensor reached a plateau immediately prior to switching in the stationary water surface test. The relation between the control signal for the laser diodes and the reliable data obtained by the optic sensor is indicated by the vertical arrows for 0.4250 ms (LD1) and 0.4375 ms (LD2) in Figure 5(b). Although removing the transitional data restricts the practical sampling rate
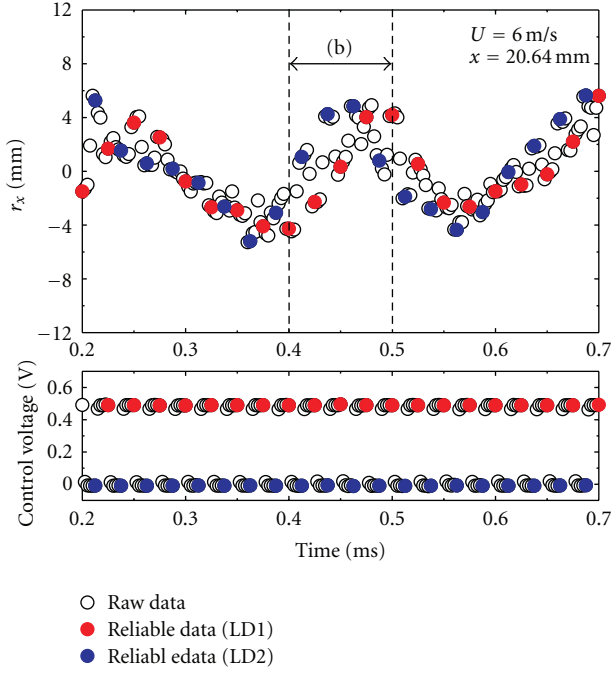
(a) Traces of data
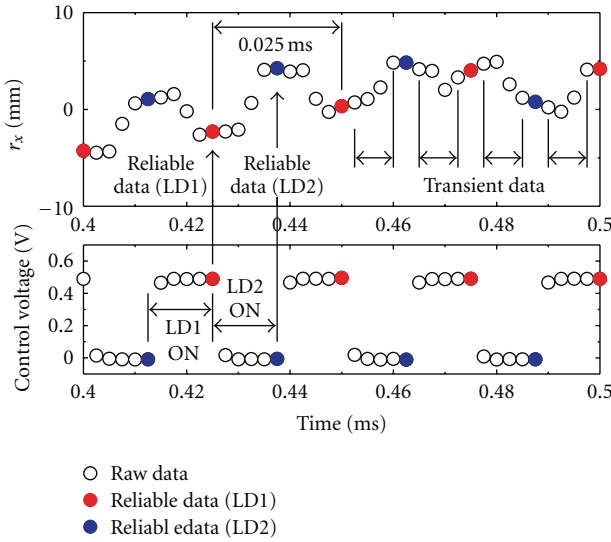
(b) Magnified trace from 0.4 ms to 0.5 ms

Figure 5: Typical streamwise displacement data obtained by two lasers.

(a)

(b)

Figure 6: Typical slope angle data and crossings detected by zero-upcrossing method.

to 40 kHz, free surface fluctuations can be observed by monitoring reliable data obtained from two measurement locations. The data acquisition time for θ_{x2} lags 0.0125 ms behind that for θ_{x1} because of the switching. In each measurement, 39 321 reliable data points are obtained per laser diode in a sampling period of 0.98 s.

The cross-correlation coefficient in (4) is calculated for each wave period extracted from the time-series data for θ_x using the zero-upcrossing method. Figure 6 shows examples of the reliable free surface slope angle data at $x = 80.63$ mm for $U = 8$ m/s. The waves are indicated by
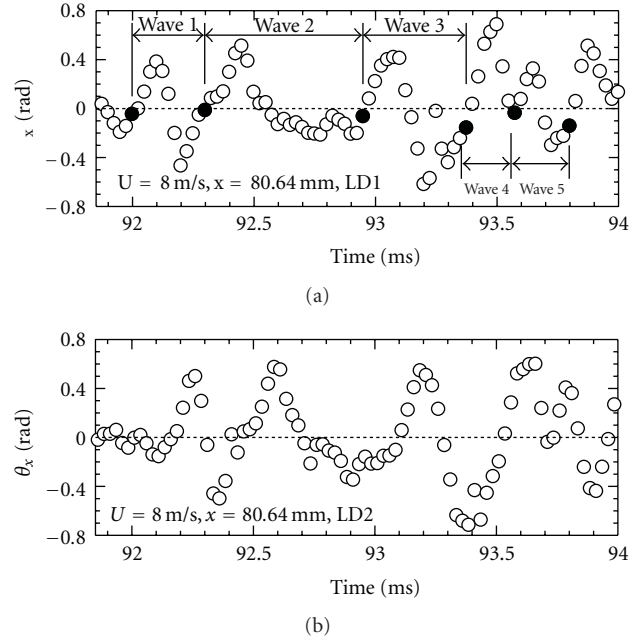
the intervals between successive crossings of the average level in the upward direction. Crossings are indicated by the solid circles in the upper figure in Figure 6. The cross-correlation coefficients are calculated for individual sequences of data between successive crossings (e.g., wave 1, wave 2, wave 3, etc. in Figure 6).

The wave speed c_x is evaluated from the dominant time lag τ_a corresponding to the maximum cross-correlation coefficient R_{max}. If the assumption of a frozen profile in (6) ceases to hold, the cross-correlation coefficient may decrease due to deformation of the waveform. Such deformed waves are eliminated when calculating statistical properties by applying a threshold; the target wave is considered to be either lost or deformed at a downstream measurement location when R_{max} is below the threshold value R_{th}. In the present study, threshold values R_{th} of $R_{max} \geq 0.90$, 0.95 and 0.98 were tested experimentally. The streamwise variation of the mean wave steepness is found to be almost independent of the tested threshold value, whereas the number of detected waves decreases with an increase in the threshold value. The results for $R_{th} = 0.90$ and 0.98 are reported in this paper.

Moreover, waves with extremely high speeds or short periods cannot be captured due to the limited time response. It is difficult to evaluate the waveform when the wave period $T(= \lambda/c_x)$ becomes smaller than the limit $T_{min} = 0.075$ ms because less than three slope angle data points are obtained over the wave period. Only waves that satisfy the condition $\lambda/c_x \geq T_{min}$ can be detected in the present experiment.

Figure 7 shows typical microflash (10 μs) pictures of the jet free surface. When $U = 6$ m/s, three distinct regions can be identified with respect to wave development in the flow direction. In the first region (0 mm $< x \leq 9$ mm),
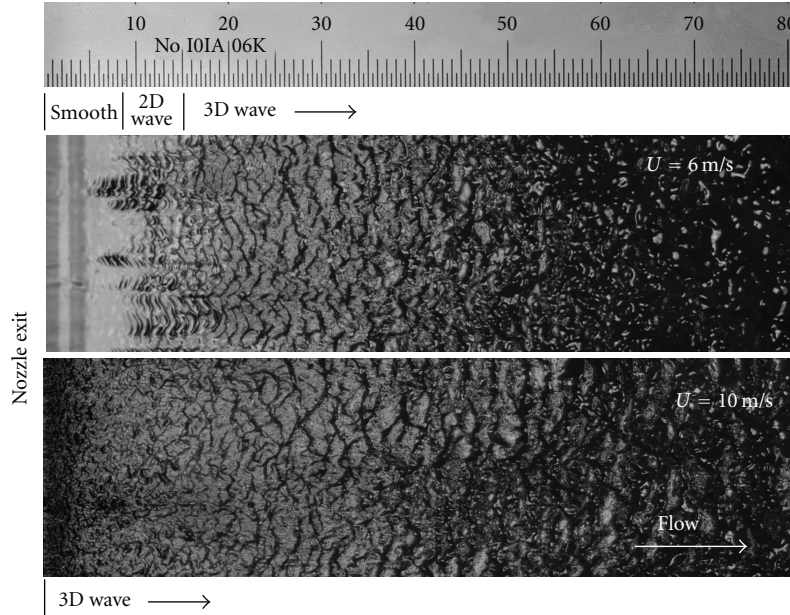
FIGURE 7: Structures on free surface of jet for $U = 6$ and $10\,\text{m/s}$.

the jet is smooth with almost no visible waves. This is followed by a second region ($9\,\text{mm} < x \le 15\,\text{mm}$) where there are 2D periodic waves with a dominant wavelength of 0.5 to 1.0 mm and wave amplitudes that increase with increasing distance x from the nozzle exit. Finally, the 2D structure of the waves decays into less regular three-dimensional (3D) wave patterns. The smooth region is characterized by intermittent time-series slope angle data [15]. The 2D wave region is distinguished by a clear peak in the power spectrum density of the slope angle fluctuations [14]. These regions are indicated in Figure 7. The smooth and 2D wave regions become shorter and eventually disappear as the jet velocity is increased. When the jet velocity exceeds ~8 m/s, capillary waves appear on the free surface of the jet immediately downstream from the nozzle exit. Linear instability analysis [21, 22] indicates that periodic wave generation is related to shear-mode instabilities under the free surface. The relaxation process in the separate nozzle-wall boundary layer may be related to the development of the 2D wave region. However, linear analysis is applicable only to the initial growth of perturbations during which the velocity gradient below the free surface is relaxed. Linear analysis applies only to the initial jet region $x \approx 1.1\,D_e$ (where D_e is the nozzle exit height) for $U \le 8\,\text{m/s}$ [14]. Linear theory is inapplicable at higher velocities ($U > 8\,\text{m/s}$) because the nozzle-exit boundary layer will exhibit transient or turbulent property. Therefore, highly nonlinear and irregular free surface waves that develop downstream of the linear amplification region near the nozzle exit or develop on the turbulent high-speed jet cannot be characterized by the theoretical prediction.

Figure 8 shows the streamwise variation of the number of identified waves, N, using the present optical technique.

N represents the number of θ_x data sets that have a cross-correlation coefficient greater than R_{th} and a wave period greater than T_{min}. Since the free surface is accelerated after exiting nozzle and capillary waves are initially generated and grow, N increases rapidly near the nozzle exit. N varies due to the local variation in the wave period and wave velocity. It reaches a steady state downstream of the point where the free surface of the jet becomes stable. At all the tested velocities, increasing the threshold R_{th} drastically reduces N. Waves with extremely high speeds or short periods also cannot be captured due to the limited time response. However, the sampling frequency could be improved by developing a detector that has a higher dynamic response rate for discontinuous beams. The required time response can be improved by increasing the distance L between the two lasers, although this would generate large uncertainties in the evaluated wave velocity.

Figure 9 shows a plot of the mean wavelength λ_{ave} (an ensemble average of N sets of wavelength data), against the distance x from the nozzle exit for different jet velocities. The dotted line indicates that the RMSD for each wavelength data point with $R_{\text{th}} = 0.90$. λ_{ave} increases with increasing x for all the velocities, and it decreases with increasing average jet velocity. For comparison, the wavelength evaluated from the luminance profile of a still photograph is plotted. 100 profiles of streamwise luminance along the center axis of the test section were extracted from photographs (see Figure 7). The wavelength was determined by the zero-upcrossing method as in the slope angle analysis. Error bars indicate the RMSD for each mean wavelength data. Since the spatial resolution of photograph is 0.035 mm per pixel, luminance analysis can detect wavelengths greater than 0.106 mm ($=\lambda_{\text{min,photo}}$) when one wavelength covers three pixels. The photograph has

(a)
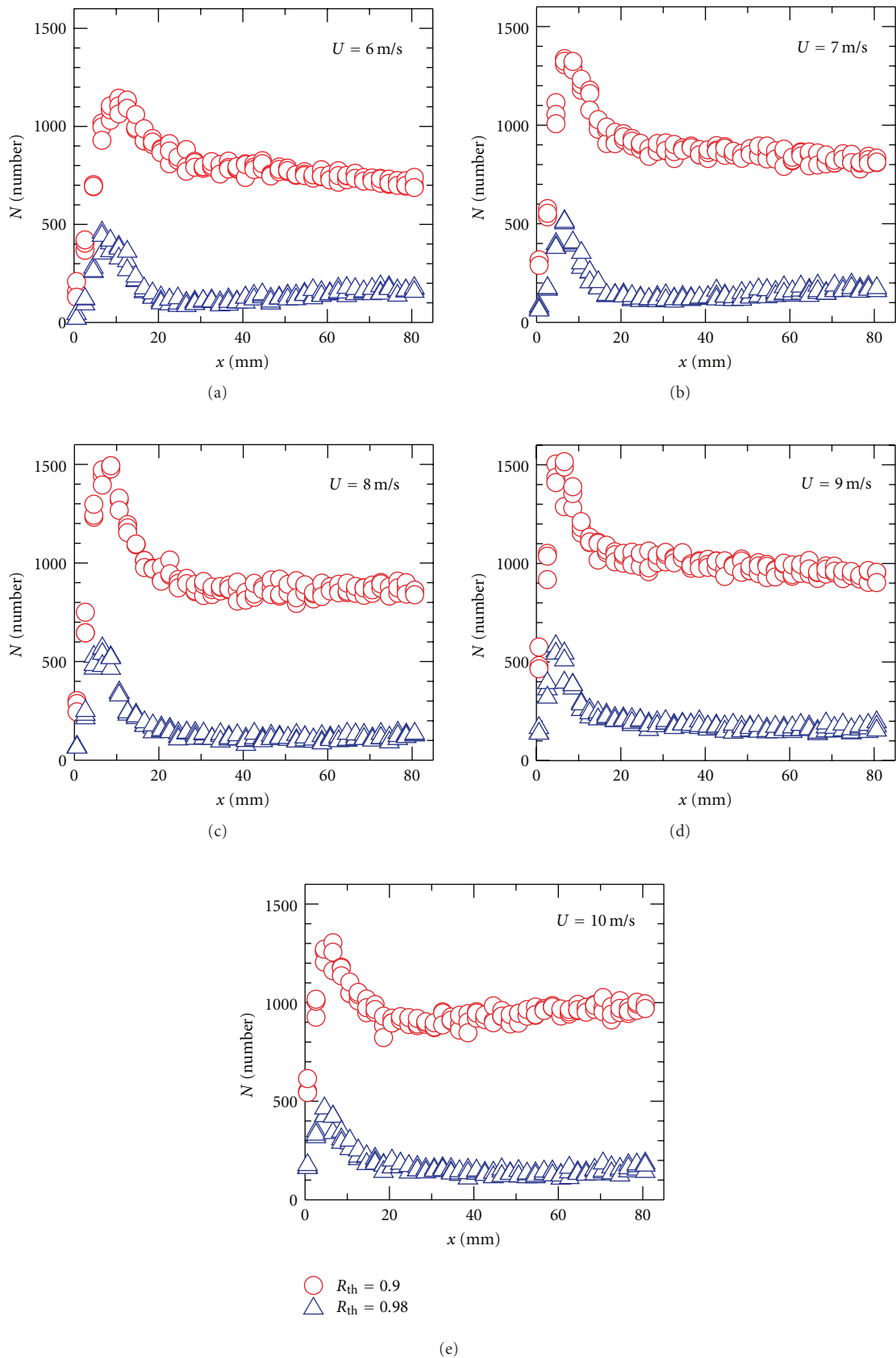
(b)

(c)

(d)

(e)

○ $R_{th} = 0.9$
△ $R_{th} = 0.98$

FIGURE 8: Number of identified free surface waves.

(a)

(b)

(c)

(d)

Laser

○ $R_{th} = 0.9$

- - - RMSD ($R_{th} = 0.9$)
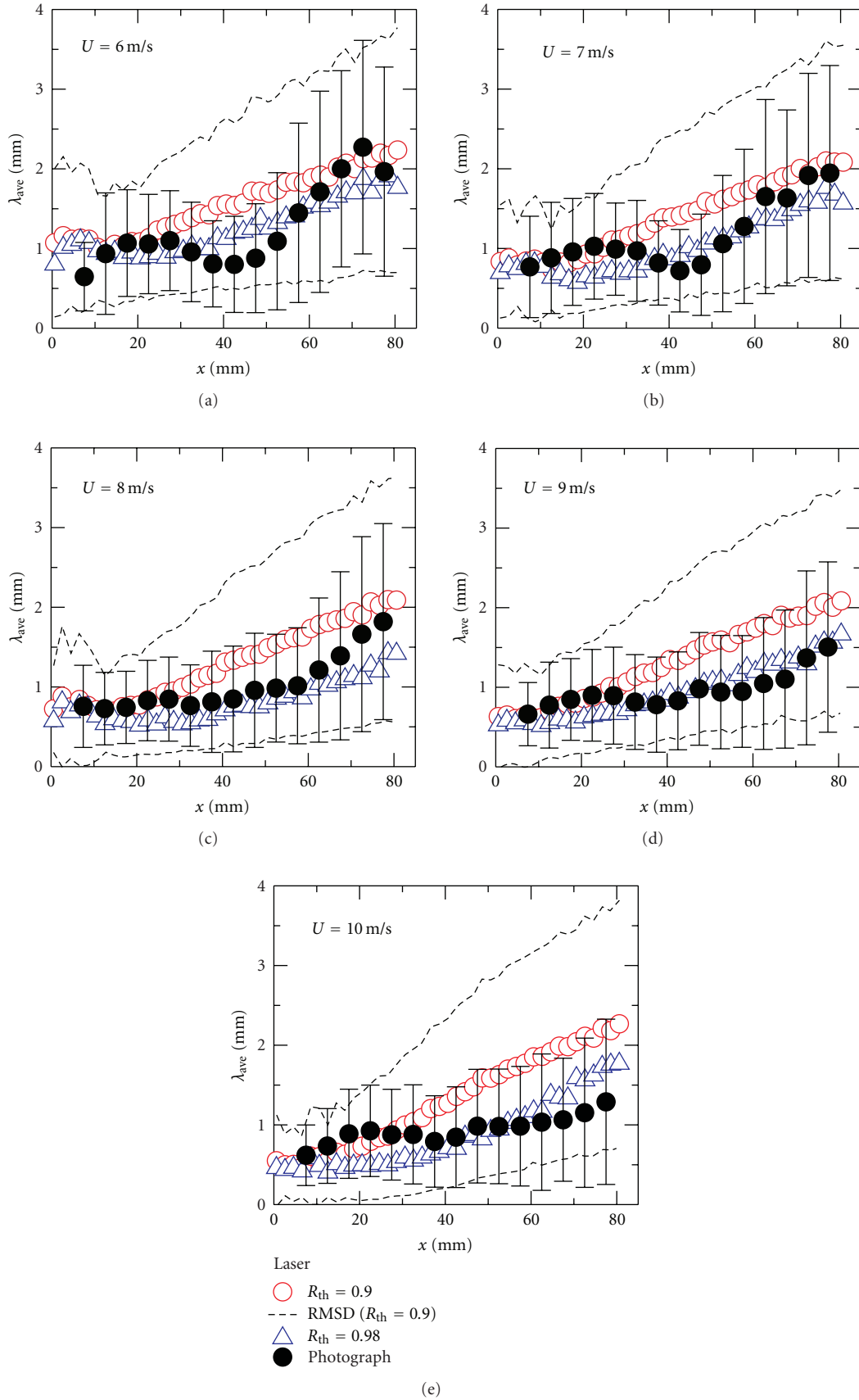
△ $R_{th} = 0.98$

● Photograph

(e)

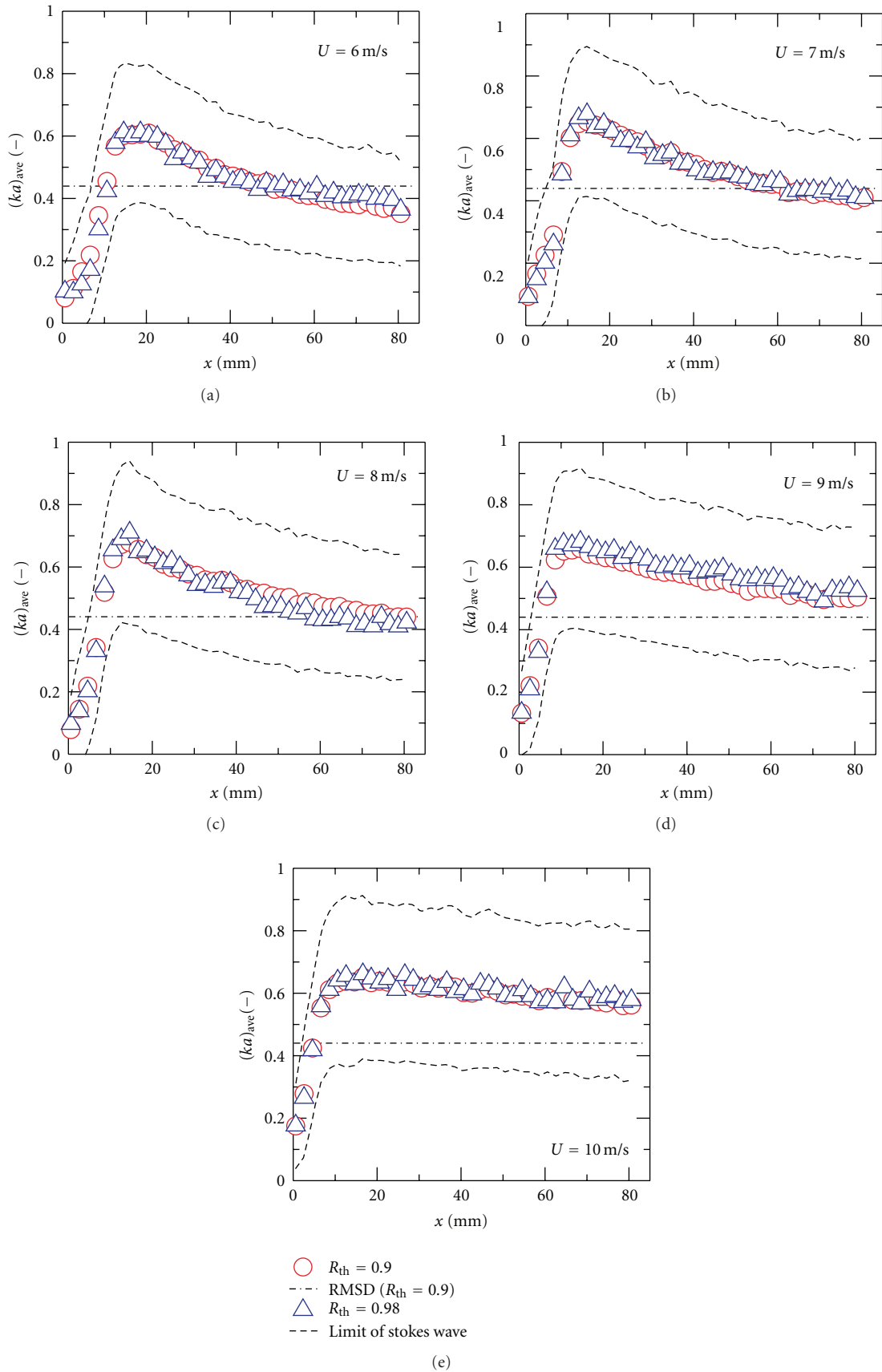FIGURE 9: Local value of mean wavelength.

(a)

(b)

(c)
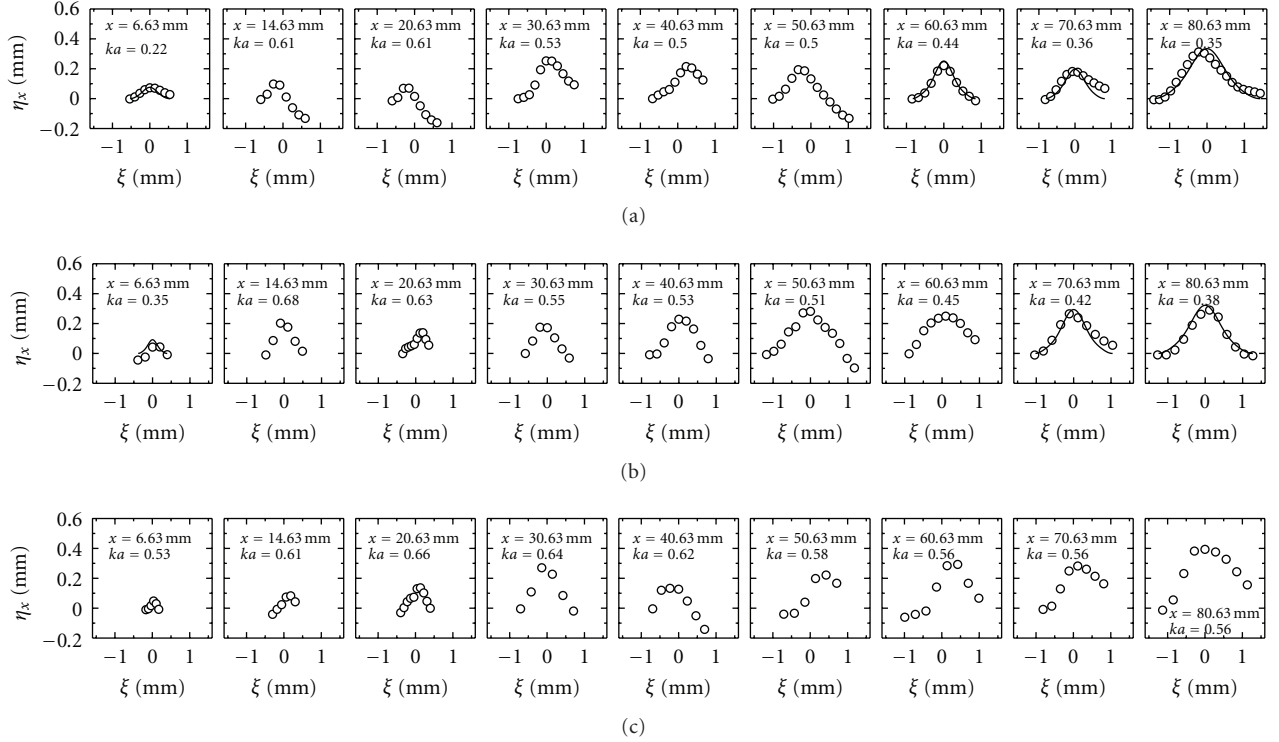
(d)

(e)

FIGURE 10: Local value of mean wave steepness.

FIGURE 11: Examples of observed waveforms for $U = 6, 8,$ and 10 m/s ($R_{th} = 0.90$).

superior resolution to the laser refraction technique when c_x is greater than 1.4 m/s ($=\lambda_{\min,\text{photo}}/T_{\min}$). Since the optical measurement cannot measure waves with extremely small periods (or deformed waves), the dominant wavelength is actually larger than that determined from the photograph. Therefore, for the higher velocities (i.e., $U = 9$ and 10 m/s), the difference between photograph and optical measurements increases with increasing x due to the loss of small wavelength data (e.g., a 0.5-mm-wavelength wave cannot be detected when it has a velocity above 6.7 m/s). An increase in R_{th} reduces the deviation because long wavelength data are eliminated due to the ambiguity in evaluating the wave velocity; in contrast, the resolution for smaller wavelengths cannot be improved. On the other hand, for the lower velocities (i.e., $U = 6, 7$ and 8 m/s), an inconsistency occurs mainly at 20 mm $\leq x \leq 60$ mm. This may be attributable to the deformation and fragmentation of waves followed by the initial growth of waves.

The mean wave steepness $(ka)_{\text{ave}}$, which is defined as the product of the wave amplitude a and the wavenumber k ($= 2\pi/\lambda$), is plotted in Figure 10. The wave amplitude is given by $a = h/2$. Since a and k are evaluated from an individual waveform η_x by integrating the set of θ_x detected by the zero-upcrossing method, $(ka)_{\text{ave}}$ is evaluated as an ensemble average for each ka for N waves.

The mean wave steepness will have a maximum at a certain distance from the nozzle exit; we had previously observed this phenomenon for $U \leq 5$ m/s [19]. The mean wave steepness near the peak exceeds the breaking limit of Stokes waves ($ka = 0.446$ [23]). This implies that

the periodic 2D wave becomes unstable near the end of its growth, and that it decays into a flatter, more stable waveform downstream for the lower velocities (i.e., $U = 6, 7,$ and 8 m/s). Since higher waves, for which the steepness of the waveform exceeds the limit for Stokes waves, are very unstable, they must decay or deform when propagating on a free surface [23]. Therefore, the mean steepness decreases further downstream. With increasing jet velocity, the growth and decay of waves cannot be explained by a linear theory. However, significantly large steepnesses were observed for the higher velocities (i.e., $U = 9$ and 10 m/s). Although measurement of high-speed and short-period waves is restricted due to the limited temporal response, the statistical properties of a free surface were exhibited when the average jet velocity exceeds 8 m/s.

Figure 11 shows examples of waveforms obtained at several locations for $U = 6, 8,$ and 10 m/s. The plot indicates the results of numerically integrating the slope angle data by substituting a particular value of c_x into (6) for a single wave. For example, the profile of η_x at $x = 80.63$ mm in Figure 11(b) indicates free surface elevation, which is evaluated by integrating the data for "wave 1" for θ_x (as shown in Figure 6). The values of ka obtained from the shape of η_x are indicated in the legend of each figure. These waves are selected so that their wavelengths and wave steepnesses are close to the local mean values, which are shown in Figures 9 and 10, respectively. Since the wave velocity c_x transforms the time axis t into a spatial axis on integrating (6), the abscissa ξ ($\equiv c_x \cdot dt$) indicates the spatial scale of the wave; $c_x \cdot dt$ indicates the distance at which the free surface moves

in the streamwise direction during the sampling period dt with velocity c_x. In Figure 11, the plots are shifted by $-\lambda/2$ in the transverse direction to center the waveforms at $\xi = 0$. It should be noted that the data in Figure 11 does not follow the same wave propagating on the free surface. It can be observed that capillary waves are generated and grow with increasing distance from the nozzle exit. The waves are steepest at $x \approx 20$ mm; they relax into moderate waveforms with a further increase in x. To emphasize the nonlinear and asymmetric form of the observed waves, the solid line indicates the third-order approximation of Stokes waves [24]; it is given by

$$k\eta = ka \cos k\xi + \frac{1}{2}(ka)^2 \cos 2k\xi + \frac{3}{8}(ka)^3 \cos 3k\xi, \quad (7)$$

where the corresponding experimental value for ka is substituted into this equation for each wave.

Some of the measured waveform agrees with the profile for Stokes waves at the downstream location where the mean wave steepness is below the limit for a Stokes wave. However, highly deformed waveforms have been observed at the higher velocities using the present optical measurement technique.

5. Conclusion

Optical measurements of free surface waves on a water jet were performed for an average jet velocity of $U \leq 10$ m/s. The present technique employs an optic sensor with one photodiode to detect the displacements of two pulsed laser beams refracted at two locations separated by 1.27 mm on the free surface of the jet. Time-series slope angle data is obtained at a rate of 40 kHz. The wave speed is evaluated from the cross-correlation coefficient for each wave. The shape of the free surface wave is evaluated by integrating the slope angle data.

The mean wavelength obtained by this technique is slightly greater than that obtained by photographic measurements because of the limited temporal response of the system that we used. However, the results demonstrate that this technique is capable of observing the linearly unpredictable free surface as variations in the mean wave steepness and the waveform.
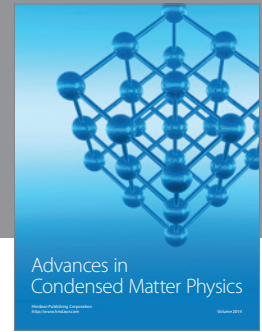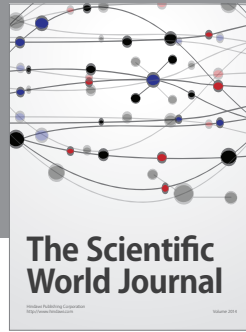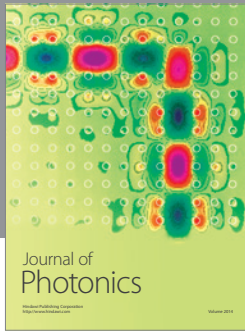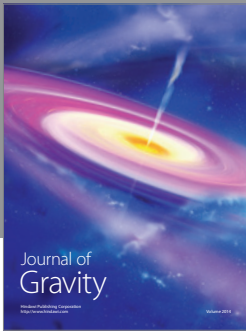
Acknowledgment

References

[1] M. J. McCready and T. J. Hanratty, "Effect of air shear on gas absorption by a liquid film," *AIChE Journal*, vol. 31, no. 12, pp. 2066–2074, 1985.

[2] L. M. Wolff and T. J. Hanratty, "Instantaneous concentration profiles of oxygen accompanying absorption in a stratified flow," *Experiments in Fluids*, vol. 16, no. 6, pp. 385–392, 1994.

[3] H. C. Kang and M. H. Kim, "The development of a flush-wire probe and calibration method for measuring liquid film thickness," *International Journal of Multiphase Flow*, vol. 18, no. 3, pp. 423–437, 1992.

[4] H. C. Kang and M. H. Kim, "Measurement of three-dimensional wave form and interfacial area in an air-water stratified flow," *Nuclear Engineering and Design*, vol. 136, no. 3, pp. 347–360, 1992.

[5] X. Zhang and C. S. Cox, "Measuring the two-dimensional structure of a wavy water surface optically: a surface gradient detector," *Experiments in Fluids*, vol. 17, no. 4, pp. 225–237, 1994.

[6] D. Dabiri and M. Gharib, "Simultaneous free-surface deformation and near-surface velocity measurements," *Experiments in Fluids*, vol. 30, no. 4, pp. 381–390, 2001.

[7] H. Ushimaru et al., "Experimental determination of jet surface configuration based on color-coding measurement of surface slope angle," in *Proceedings of the 13th International Topical Meeting on Nuclear Reactor Thermal Hydraulics (NURETH '09)*, Kanazawa, Japan, September-October 2009.

[8] H. Kondo, T. Kanemura, N. Yamaoka et al., "Measurement of free surface of liquid metal lithium jet for IFMIF target," *Fusion Engineering and Design*, vol. 82, no. 15–24, pp. 2483–2489, 2007.

[9] B. Zhang, Y. He, Y. Song, and A. He, "Deflection tomographic reconstruction of a complex flow field from incomplete projection data," *Optics and Lasers in Engineering*, vol. 47, no. 11, pp. 1183–1188, 2009.

[10] L. U. Lilleleht and T. Hanratty, "Measurement of interfacial structure for co-current air-water flow," *The Journal of Fluid Mechanics*, vol. 11, pp. 65–81, 1961.

[11] H. Hashimoto and T. Suzuki, "Experimental and theoretical study of fine interfacial waves on thin liquid sheet," *JSME International Journal, Series 2*, vol. 34, no. 3, pp. 277–283, 1991.

[12] F. Yoshino, T. Hayashi, and K. Urata, "Measurement of two-dimensional wave of shallow-water flow on circular cylinder," in *Proceedings of the ASME/JSME Fluids Engineering and Laser Anemometry Conference and Exhibition*, pp. 225–255, August 1995.

[13] S. R. Duke, L. M. Wolff, and T. J. Hanratty, "Slopes of small-scale wind waves and their relation to mass transfer rates," *Experiments in Fluids*, vol. 19, no. 4, pp. 280–292, 1995.

[14] K. Itoh, Y. Tsuji, H. Nakamura, and Y. Kukita, "Initial free surface instabilities on a high-speed water jet simulating a liquid-metal target," *Fusion Technology*, vol. 36, no. 1, pp. 69–84, 1999.

[15] K. Itoh et al., "Influence of the development history of nozzle wall boundary layer upon wave generation on a liquid jet free surface," *Journal of Fluid Science and Technology*, vol. 4, no. 3, pp. 512–523, 2009.

[16] R. Savelsberg, AD. Holten, and W. Van De Water, "Measurement of the gradient field of a turbulent free surface," *Experiments in Fluids*, vol. 41, no. 4, pp. 629–640, 2006.

[17] R. Savelsberg and W. van de Water, "Experiments on free-surface turbulence," *Journal of Fluid Mechanics*, vol. 619, pp. 95–125, 2009.

[18] D. Snouck, M. T. Westra, and W. van de Water, "Turbulent parametric surface waves," *Physics of Fluids*, vol. 21, no. 2, Article ID 025102, 2009.

[19] K. Itoh et al., "Optical measurement of the instantaneous wavy surface structure on a water plane jet," *Journal of Physics: Conference Series*, vol. 147, no. 1, Article ID 012046, 2009.

[20] H. Bazargan, H. Bahai, and F. Aryana, "Simulation of the mean zero-up-crossing wave period using artificial neural networks trained with a simulated annealing algorithm," *Journal of Marine Science and Technology*, vol. 12, no. 1, pp. 22–33, 2007.

[21] C. Brennen, "Cavity surface wave patterns and general appearance," *The Journal of Fluid Mechanics*, vol. 44, pp. 33–49, 1970.

[22] K. Itoh et al., "Linear stability analysis on free-surface liquid jet with different simplification of velocity profile," *Journal of Fluid Science and Technology*, vol. 2, no. 2, pp. 417–428, 2007.

[23] W. K. Melville, "The role of surface-wave breaking in air-sea interaction," *Annual Review of Fluid Mechanics*, vol. 28, pp. 279–321, 1996.

[24] A. D. D. Craik, "George Gabriel stokes on water wave theory," *Annual Review of Fluid Mechanics*, vol. 37, pp. 23–42, 2005.